Research in Astron. Astrophys. **2010** Vol. **10** No. **8**, 713–736
http://www.raa-journal.org *http://www.iop.org/journals/raa*

***R**esearch in*
***A**stronomy and*
***A**strophysics*

INVITED REVIEWS

Mars geodesy, rotation and gravity

Pascal Rosenblatt[1] and Veronique Dehant[2]

[1] Royal Observatory of Belgium, 3 Avenue Circulaire, B1180 Brussels, Belgium; *rosenblatt@oma.be*
[2] Royal Observatory of Belgium; *dehant@oma.be*

Received 2010 March 11; accepted 2010 April 5

Abstract This review provides explanations of how geodesy, rotation and gravity can be addressed using radioscience data of an orbiter around a planet or of the lander on its surface. The planet Mars is the center of the discussion. The information one can get from orbitography and radioscience in general concerns the global static gravitational field, the time variation of the gravitational field induced by mass exchange between the atmosphere and the ice caps, the time variation of the gravitational field induced by the tides, the secular changes in the spacecraft's orbit induced by the little moons of Mars named Phobos and Deimos, the gravity induced by particular targets, the Martian ephemerides, and Mars' rotation and orientation. The paper addresses as well the determination of the geophysical parameters of Mars and, in particular, the state of Mars' core and its size, which is important for understanding the planet's evolution. Indeed, the state and dimension of the core determined from the moment of inertia and nutation depend in turn on the percentage of light elements in the core as well as on the core temperature, which is related to heat transport in the mantle. For example, the radius of the core has implications for possible mantle convection scenarios and, in particular, for the presence of a perovskite phase transition at the bottom of the mantle. This is also important for our understanding of the large volcanic province Tharsis on the surface of Mars.

Key words: planets and satellites: Mars — variables: rotation, gravity, and interior of Mars

1 INTRODUCTION

Mars has been an important planet in the exploration of our solar system. There have been missions to Mars dating back to the Sixties. Several flybys of Mars (e.g. Mars 4, and Mariner 4, 6 and 7 missions), orbiters around Mars (e.g. Mars 3, 5 and 6, Mariner 9 and Viking 1 and 2 missions) and landers on Mars (Mars 3 and 6 and Viking 1 and 2 missions) were sent prior to 1975. There was an orbiter, Phobos 2, in 1988, and then nothing before 1997. Starting at that time, there was again roughly one launch at each possible window, among which were the launches of the Mars Global Surveyor (MGS) in 1997, Mars Odyssey (ODY) in 2001, Mars Express (MEX) in 2003 (the first European mission to Mars), Mars Exploration Rovers (MERs, Spirit and Opportunity) also in 2003, Mars Reconnaissance Orbiter (MRO) in 2005, and Phoenix in 2007, which have allowed us to learn a lot about Mars' history, interior, surface, and atmosphere. Future missions to Mars, such

Table 1 Range of Frequencies for the Different Frequency Bands used in Radioscience

Frequency Band	Uplink	Downlink
UHF	[390 MHz, 405 MHz]	[435 MHz, 450 MHz]
S-band	[2.026 GHz, 2.11 GHz]	[2.2 GHz, 2.29 GHz]
X-band	[7.145 GHz, 7.19 GHz]	[8.4 GHz, 8.45 GHz]
Ka-band	[34.2 GHz, 34.7 GHz]	[31.8 GHz, 32.3 GHz]

Fig. 1 DSN 70 m station.

as the Mars Science Laboratory (MSL) in 2011, Phobos Grunt and Yinghuo-1 in 2011, or MAVEN (Mars Atmosphere and Volatile Evolution Mission) in 2013, and ExoMars (2016–2018), will further complement our knowledge of Mars. In addition to providing information on the geology of Mars (Rossi & van Gasselt 2010), some of these past spacecraft and some of the future spacecraft have also allowed and will allow for some geodesy of the planet Mars (including its two small moons Phobos and Deimos) to take place.

Mars geodesy mainly addresses gravity and rotation, from which properties of the interior of Mars can be deduced. The observations that are used for this are radio signals in UHF, S-band, X-band, or Ka-band. The frequency ranges for these radio bands which are reserved for the space radio link to Mars are presented in Table 1. The measurements used for reaching the geodesy objectives are the Doppler shifts and ranging times as measured at the Deep Space Network (DSN) stations of NASA or the ESTRACK ESA tracking stations of ESA. These ground stations are huge antennas with diameters of 34 m or 70 m, as presented in Figure 1. The Doppler shifts are measurements of the shifts in the frequency induced by the relative position between the transmitter and receiver (see Fig. 2). These shifts are measured over a certain period of time called the integration time.

For a one-way link between the spacecraft and Earth's station (see Fig. 3), the measured Doppler shift can be written as (Moyer 2000)

$$\Delta f = \frac{f_{\mathrm{T}}}{cT_{\mathrm{c}}} \left[\rho(t_2) - \rho(t_1)\right], \tag{1}$$

where, for the example of a spacecraft-Earth radio link, f_{T}, is the frequency transmitted at the spacecraft, c is the speed of light, and $\rho(t_1)$ and $\rho(t_2)$ are the spacecraft-station ranges at the start-time (t_1) and end-time (t_2) of the Doppler count time T_{c}, respectively.

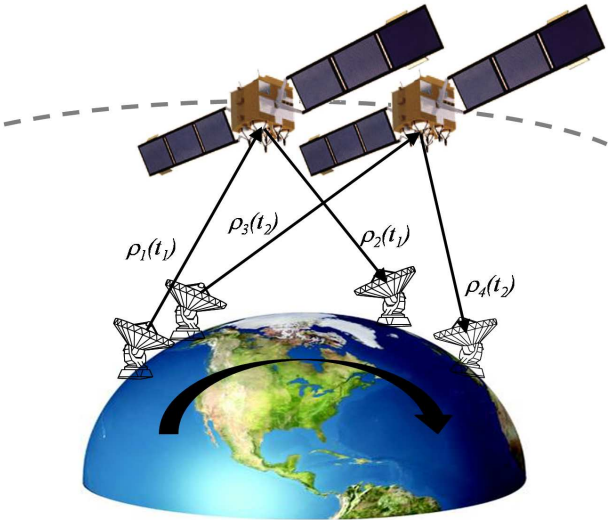

Fig. 2 Measurements over a particular integration time.

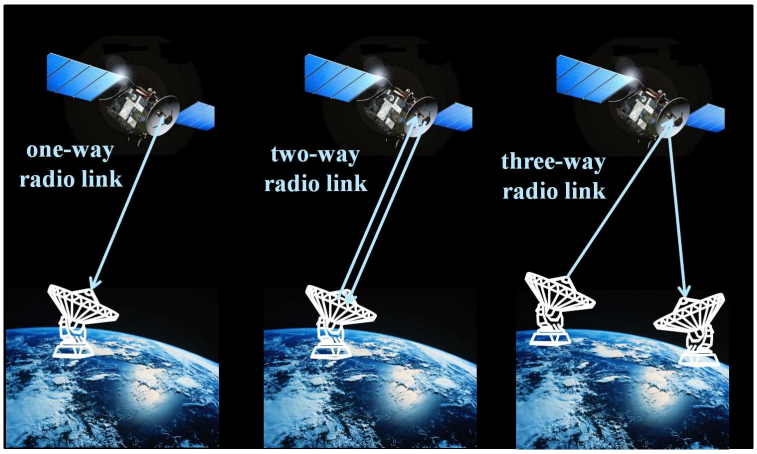

Fig. 3 Representation of the one-way, two-way and three-way radio links.

For a signal transmitted from Earth to the spacecraft (uplink path) and then received back on Earth (downlink path), corresponding to a two-way link (see Figs. 2 and 3), we have (Moyer 2000)

$$\Delta f = \frac{M_{\mathrm{T}} f_{\mathrm{T}}}{c T_{\mathrm{c}}} \left[\rho_3(t_2) + \rho_4(t_2) - \rho_1(t_1) - \rho_2(t_1)\right], \tag{2}$$

where f_{T} is the frequency transmitted at the ground station to the spacecraft, ρ_1 and ρ_3 are the spacecraft-station ranges of the uplink paths, ρ_2 and ρ_4 are the spacecraft-station ranges of the downlink paths, and t_1 and t_2 are the start-time and end-time of the Doppler count at the ground station. The ranging measurements consist of time intervals between the signal sent to the spacecraft and that received at the ground station, and M_{T} is the transponder factor (e.g. 880/749 for an X-band two-way link).

From Doppler and/or ranging measurements, one is able to reconstruct the motion of a spacecraft around Mars or of a lander or a rover with respect to the Earth. One can, as well, measure the relative motion of a lander or a rover with respect to a spacecraft. The radio signals are often used as a "two-way" signal (see Fig. 3). For a two-way, the reference frequency is on Earth, the signal is received at Mars, and coherently transponded back to Earth; the Doppler and ranging are then measured on Earth. In this configuration, the Earth's station is the same for emission and reception of the signal. The "three-way" configuration is sometimes used too, and in this case, the receiving station is different from the transmitting station. The "three-way" ranging needs, however, to correct for the offset between the clocks at the two stations. One also sometimes uses an Ultra-Stable Oscillator (USO) aboard the spacecraft for generating the signal and then receiving it on Earth; this is the so-called "one-way" radio tracking. The precision of the measurements will then be limited by the stability of the USO. Mainly two-way Doppler and ranging are used for radioscience scientific applications. The geometry, or equivalently the orientation of the line-of-sight, changes during the mission. When the spacecraft's orbital plane is perpendicular to the line-of-sight, the orbit is viewed "face-on" from the Earth and when the orbital plane is seen from the tranche, or equivalently when the line-of-sight is in the orbital plane, the orbit is viewed "edge-on" from the Earth, as shown in Figure 4.

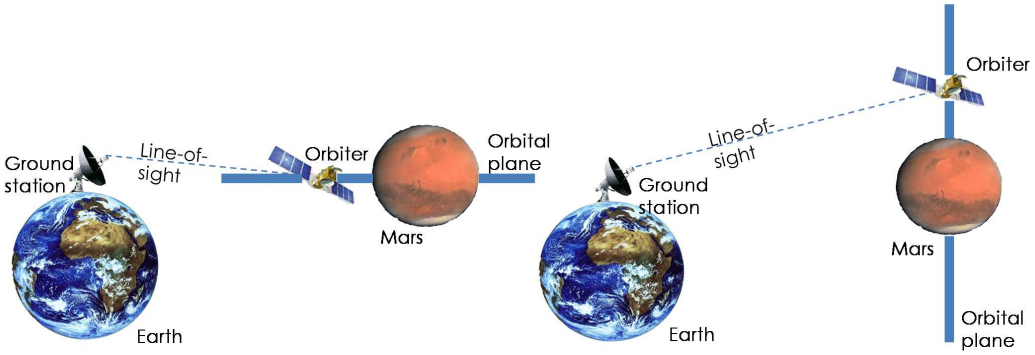

Fig. 4 Geometry of the spacecraft's orbit over the course of a mission; *left*: edge-on; *right*: face-on.

The different ways envisaged in radioscience involve the Earth-based ground stations, the orbiter and the lander or the rover. The radio links are shown in Figure 5. All these radio links provide information on the global orbit of the spacecraft and its changes in space and time (precise orbit positioning), gravitational and non-gravitational perturbations of the spacecraft trajectory, the acceleration undergone by the spacecraft at a particular space and time (on targets), and the Mar's orientation and rotation parameters (the so-called MOP). This paper will thus deal with the information one can get from orbitography and radioscience in general concerning the global static gravitational field (Sect. 2), the time variation of the gravitational field induced by the mass exchange between the atmosphere and the ice caps (Sect. 3), the time variation of the gravitational field induced by the tides (Sect. 4), the secular changes in the spacecraft's orbit induced by the little moons of Mars, Phobos and Deimos (Sect. 5), the gravity induced by particular targets (Sect. 6), Martian ephemerides (Sect. 7), and Mars' rotation and orientation (Sect. 8). The determination of the geophysical parameters of Mars and the science addressed by radioscience are explained in Section 9.

2 GLOBAL STATIC GRAVITATIONAL FIELD

When a spacecraft is in orbit around a planet, it feels the gravitational field of the planet (in addition to the gravitational field of the Sun and the moon(s) orbiting the planet and, to a minor extent, of the

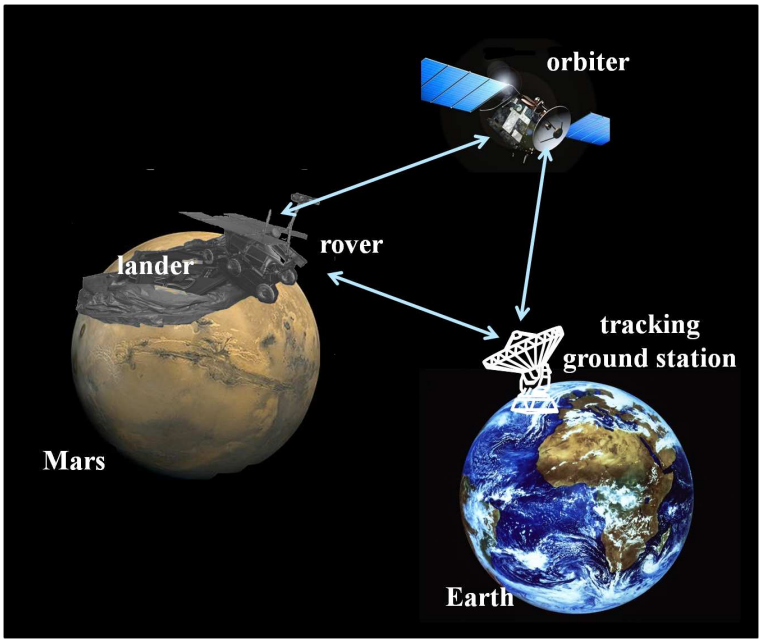

Fig. 5 Different radio links between the Earth, Mars and an orbiter around Mars.

other planets, see Sect. 6). This gravitational field is due to all the masses inside the planet. If the planet is homogeneous and spherical, the gravitational field would be equivalent to that of a point mass, and the orbital motion of the spacecraft due to this gravitational field would follow Keplerian motion. However, a planet like Mars, is not spherical, the masses inside are heterogeneously distributed, and the planet rotates. The most useful representation of the planetary gravitational potential U is as a series of spherical harmonics, written at each point P located at the exterior of the planet as follows:

$$U = \frac{GM}{R} + \frac{GM}{R} \sum_{l=2}^{L} \left(\frac{R}{r}\right)^{l} \sum_{m=0}^{l} \left(C_{lm} \cos m\lambda + S_{lm} \sin m\lambda\right) P_{lm}(\sin \phi), \tag{3}$$

where G is the gravitational constant, M is the mass and R the equatorial reference radius of the planet, C_{lm} and S_{lm} are dimensionless harmonic coefficients of degree l and order m, the P_{lm}'s are the Legendre functions of the first kind (Legendre polynomials when $m = 0$), and r, ϕ, and λ are the spherical coordinates of the point P in a reference system fixed with respect to the planet. The summation over the degree l, which starts at degree 2 if one assumes that the origin of the reference system coincides with the planet's center of mass, is in principle infinite, but it is in practice truncated to a maximum degree and order L. This truncation is predetermined by sensitivity analysis based on the orbital characteristics and tracking system capabilities (e.g. Marty et al. 2009). The first term on the right-hand side of Equation (3) represents the central term of the potential and generates the Keplerian motion of the orbiter, and the second term represents the perturbing potential U_{p}, which generates perturbations of this Keplerian orbit. The Keplerian orbit and its perturbations are

described by the Lagrange planetary equations

$$
\begin{aligned}
\frac{da}{dt} &= \frac{2}{na}\frac{\partial U_{\mathrm{p}}}{\partial M},\\
\frac{de}{dt} &= -\frac{\sqrt{1-e^2}}{na^2 e}\frac{\partial U_{\mathrm{p}}}{\partial \omega} + \frac{1-e^2}{na^2 e}\frac{\partial U_{\mathrm{p}}}{\partial M},\\
\frac{di}{dt} &= \frac{-1}{na^2\sqrt{1-e^2}\sin i}\frac{\partial U_{\mathrm{p}}}{\partial \Omega} + \frac{\cos i}{na^2\sqrt{1-e^2}\sin i}\frac{\partial U_{\mathrm{p}}}{\partial \omega},\\
\frac{d\Omega}{dt} &= \frac{1}{na^2\sqrt{1-e^2}\sin i}\frac{\partial U_{\mathrm{p}}}{\partial i},\\
\frac{d\omega}{dt} &= \frac{\sqrt{1-e^2}}{na^2 e}\frac{\partial U_{\mathrm{p}}}{\partial e} + \frac{\cos i}{na^2\sqrt{1-e^2}\sin i}\frac{\partial U_{\mathrm{p}}}{\partial i},\\
\frac{dM}{dt} &= n - \frac{2}{na}\frac{\partial U_{\mathrm{p}}}{\partial a} + \frac{1-e^2}{na^2 e}\frac{\partial U_{\mathrm{p}}}{\partial e},
\end{aligned}
\tag{4}
$$

where n is the mean motion of the orbiting spacecraft (Keplerian motion), and a, e, i, Ω, ω, and M are the Keplerian elements, respectively, the semi-major axis, the eccentricity, the inclination, the longitude of the node of the orbit, the longitude of the perigee, and the mean anomaly (see Fig. 6).

The theory of perturbations has provided solutions for the Lagrange equations. One of the most useful solutions has been given by Kaula (1966). In this solution, the perturbing gravitational potential U_{p} is developed as a function of the Keplerian elements (see eqs. (3.70) and (3.71) in Kaula, 1966), then the Lagrange equations are solved using an iterative two-step method: the first step consists of solving the secular variations and the second step consists of solving the periodic variations of the orbital elements. The former variations correspond to the precession of the orbit: secular changes of the longitude of the node of the orbit, of the longitude of the perigee, and of the mean anomaly, while the other three elements do not vary. The orbital precession is the major perturbation of the Keplerian motion, and is proportional to the J_2 (with $J_2 = -C_{20}$), i.e. the first even zonal harmonic of the potential. Note that if one reduces the expression of the perturbing potential to the single J_2 harmonic, it corresponds, in the first order (ignoring the internal dynamical effects on the

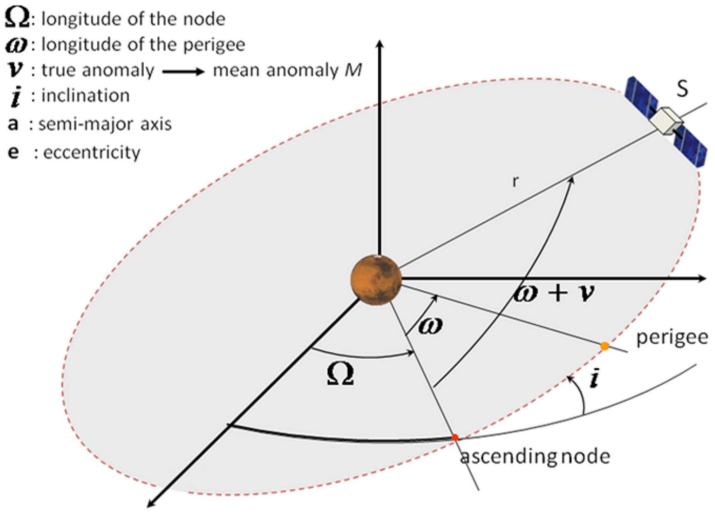

Fig. 6 Keplerian elements of the orbit.

moments of inertia), to a planet in rotation and in hydrostatic equilibrium as depicted by Clairaut's equations (J_2 is proportional to the difference between the polar moment of inertia (C) and the equatorial moment of inertia (A), and represents the dynamical flattening of the planet; it is called the *form factor*). The secular drift of the precessing orbit is given by the rates of secular variations of Ω, ω, and M, which depend only on the values of J_2, R, a, and on e and i through the inclination and eccentricity functions, respectively (see eq. (3.74) in Kaula, 1966). The even zonal harmonics of higher degree (J_4, J_6, ...) also contribute to the secular drift of the orbit, so that the secular rates of Ω, ω, and M are proportional to a combination of all even zonal harmonics and do not only depend on J_2. However, the contribution of the higher order even harmonics to the orbital drift is generally lower than the J_2 contribution, because these even harmonics have values lower than the J_2 value by at least three orders of magnitude. In addition, the secular rate is proportional to $(R/a)^l$, thus the contribution of a given zonal harmonic of degree l decreases rapidly with increasing degree.

The periodic variations are superimposed on the secular motion and affect all the associated orbital elements. All gravitational harmonics contribute to these periodic variations. For example, the zonal harmonic J_2 also generates short periodic variations in the semi-major axis. The periods of these perturbations depend on the secular rates of the precessing orbit and on the rotation rate of the planet. The associated amplitudes are decreasing from longer to shorter periods. The theory of Kaula easily allows calculating the contribution of each of the harmonics to the amplitudes of all these orbital perturbations (see eq. (3.76) in Kaula, 1966), and deriving their contribution to the spacecraft velocity perturbations (see Fig. 7).

As shown in Figure 7, the gravitational velocity perturbations are on the order of a few mm s^{-1} for the MGS and ODY Martian spacecraft orbiting at an altitude of about 400 km above the planetary surface. These velocity perturbations decrease with increasing degree and order (as depicted by the black dotted line on Fig. 7), i.e. from long to short wavelength components of the gravitational field. This behavior comes from the R/r ratio to the power l in the expression of the potential (see Eq. (3)). As a consequence, the spacecraft motion's sensitivity to the short wavelengths of the planetary gravitational field depends on the altitude of the spacecraft's orbit; the lower the altitude is, the more sensitive to the short wavelengths the spacecraft's velocity perturbations are. In turn, the minimal orbital altitude provides a theoretical estimation of the maximum degree of the gravitational field solution that can be calculated. Since there is a direct correlation between Mars' topography and gravitational potential, as the altitude of a spacecraft around Mars roughly represents the minimum wavelength that can be reached in terms of the topography mass anomaly effect on the spacecraft, and as the wavelength of a harmonic is roughly inversely proportional to its degree, the maximum degree and order of the gravitational potential field solution is roughly related to the altitude of the spacecraft (this relationship is known as the Kaula's rule of thumb). In practice, the maximum degree L of the gravitational field solution also depends on the precision of the tracking system's capabilities (typically 0.1 mm s^{-1} for the X-band Doppler tracking data). The comparison between the MGS/ODY orbit's sensitivity to Mars' gravitational field and the Doppler noise level yields $L \approx 90$ (see Fig. 7). Kaula's solution of the Lagrange equations also permits an emphasis on several harmonics, which produce higher velocity perturbations than expected from their degree l and order m. This corresponds to a phenomenon of 'resonance' involving the Ω, ω, and M secular rates and the rotation rate of the planet (see eq. (3.76) in Kaula, 1966). The harmonics related to this phenomenon are clearly seen in Figure 7. The solution of Kaula also tells us that each secular and each periodic perturbation does not depend on a single gravity harmonic but on a linear combination of harmonics of several degrees, or a lumped harmonic (like the even zonal harmonic combination for the secular perturbations, see Sect. 2). Therefore, given fixed orbital characteristics, one can only access the *lumped* harmonic and not each harmonic involved in the *lumped* combination.

The analytical solutions of the planetary Lagrange equations, like Kaula's solution, have shown how the orbital motion is perturbed by the harmonics of the static gravitational field. In turn, the monitoring of this perturbed orbital motion allows retrieval of the harmonics C_{lm} and S_{lm}, which

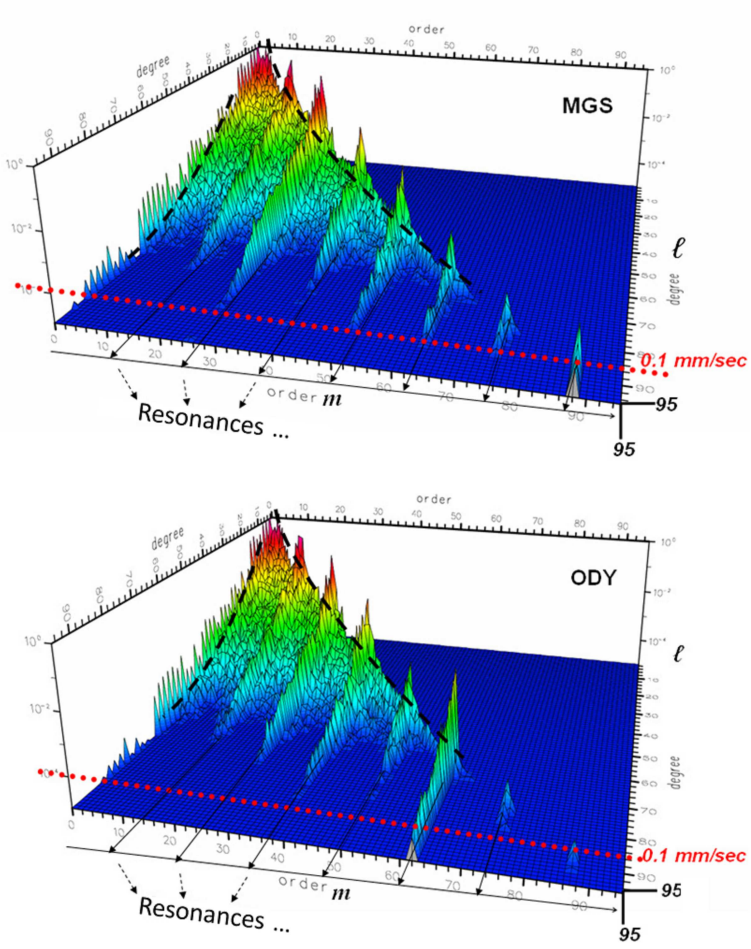

Fig. 7 Diagram of Mars' gravity orbital effects on the Mars Global Surveyor (MGS) and Mars Odyssey (ODY) spacecraft (linear theory of Kaula), shown as velocity perturbations for C_{lm}, S_{lm} pairs. The color scale is for the decimal logarithm of the perturbation in m s^{-1}. The 0.1 mm s^{-1} dotted line corresponds to about twice the ultimate capabilities of the tracking system in the X-band (from Marty et al. 2009).

correspond to a solution of the gravity of the planet. In practice, a least squares fit of the orbital motion to the Doppler tracking data is performed. This method of gravitational field determination is called the method of perturbations, and it needs to perform a Precise Orbit Determination (POD) of the spacecraft motion in order to separate as precisely as possible the gravitational perturbations from all other perturbations of non-gravitational origin. A numerical integration of the spacecraft motion is performed by modeling the measured velocity perturbations (which are the velocity perturbations projected on the orbiter-Earth Line-Of-Sight (LOS)) and by modeling all the gravitational and non-gravitational forces acting on the spacecraft (e.g. Konopliv et al. 2006; Rosenblatt et al. 2008a; Marty et al. 2009; Rosenblatt et al. 2010, in preparation). These non-gravitational forces are exerted on the faces of the spacecraft (the bus, the solar panels and the high gain antenna) and are the radiation pressure (exerted by the light emitted by the Sun as well as the reflected light and

the thermal infra-red emission of the planet), and the atmospheric drag generated by the upper atmosphere of the planet (at the low-altitude part of the spacecraft orbit, typically below 700 km for Mars). In order to maintain the spacecraft's attitude, specific maneuvers have to be performed on a regular basis (Angular Momentum Desaturation or Wheel-Off-Loading of the inertial wheels). These maneuvers generate an additional acceleration for the spacecraft, which must also be taken into account. A detailed description of the non-gravitational force modeling is given in Konopliv et al. (2006), Rosenblatt et al. (2008a,b), and Marty et al. (2009). Nevertheless, a perfect modeling of these forces cannot be achieved and some of them have to be estimated (or scaled) during the least squares fitting process to the tracking data in addition to the gravitational field harmonics. The fit of the non-gravitational forces can only be performed by evaluating a scaling of these forces with respect to their initial modeled value. In addition to the fit of parameters of the force model, parameters related to the tracking data themselves are also estimated to account for the imperfect knowledge of instrumental biases (due, for example, to the shift between the position of the spacecraft's center of mass and the position of the center of phase of its antenna) as well as of the position of the tracking stations and of the planets, which are used to model their gravitational attraction on the spacecraft (for this latter parameter, see Sect. 6). There are resulting imperfections in the retrieval of the spacecraft orbital perturbations from this fitting process, which in turn degrade the retrieval of the weaker signal of the shorter wavelengths of the gravitational field (for example, see fig. 4 in Marty et al. 2009). In spite of these limitations, solutions of Mars' static gravitational field have been obtained and are used to probe the shallower interior of planets in order to provide new constraints on the local structure of the crust and lithosphere (see Wieczorek 2007, for a useful review, and see Sect. 5).

3 TIME VARIATION OF THE GRAVITATIONAL FIELD RELATED TO CO_2 SUBLIMATION/CONDENSATION

About one fourth of the atmosphere of Mars is participating in the sublimation and condensation process of CO_2 in the atmosphere and ice caps. Mars' atmospheric CO_2 seasonal cycle induces this mass exchange between the polar caps and the atmosphere, which in turn induces seasonal variations in the gravitational potential as well as in the rotation rate of the planet (see Sect. 8). The expected contributions to the gravity's zonal harmonic variations of degree 2 to 5 (δC_{20} to δC_{50}) are on the order of a few hundredths of a percent of their static values as expected from the Global Circulation Model (GCM) of Mars' atmosphere (Smith et al. 1999; Karatekin et al. 2006a; Sanchez et al. 2006). In turn, this small amplitude in the zonal harmonic variations generates small orbital perturbations, which need an accurate reconstruction of the orbiter motion to be detected. The orbit of MGS and ODY are determined at an accuracy of about 1–2 and only the odd harmonic variations have been estimated with sufficient precision (Konopliv et al. 2006; Marty et al. 2009). In addition, the contribution of each zonal harmonic cannot be properly separated and only the lumped zonal harmonic variations can be determined (Smith et al. 2009).

Kaula's solution of the planetary Lagrange equations permits us to calculate how these fine variations in Mars' gravitational field perturb the near-polar and near-circular orbits of the MGS and ODY spacecraft. For such orbits, the main perturbations apply to the Ω, e, and ω Keplerian elements and are given by the following relationships (e.g. Yoder et al. 2003; Konopliv et al. 2006):

$$\begin{aligned} \frac{d\Omega}{dt} &= \frac{3n\cos i}{2}\left(\frac{R}{a}\right)^2 \delta C_{\mathrm{even}}, \\ \frac{dp}{dt} + i\omega_0 p &= -\frac{3n\sin i}{2}\left(\frac{R}{a}\right)^3 \delta C_{\mathrm{odd}}, \end{aligned} \tag{5}$$

with $p = e\ \mathrm{e}^{-j\omega}$, $j^2 = -1$, and $\omega_0 = -3n(R/a)^2 f_3 \delta C_{20}$. Here, δC_{even} and δC_{odd} are the even and odd lumped zonal harmonic variations, respectively, such as

$$\begin{aligned} \delta C_{\mathrm{even}} &= \delta C_{20} + f_4 \delta C_{40}, \\ \delta C_{\mathrm{odd}} &= f_3 \delta C_{30} + f_5 \delta C_{50}, \end{aligned} \tag{6}$$

where f_3 to f_5 are the coefficients of the lumped combinations (or lumped coefficients)

$$\begin{aligned} f_3 &= \frac{5}{4}\sin^2 i - 1, \\ f_4 &= \frac{5}{8}\left(\frac{R}{a}\right)^2 (7\sin^2 i - 4), \\ f_5 &= \frac{5}{16}\left(\frac{R}{a}\right)^2 (8 - 28\sin^2 i + 21\sin^4 i). \end{aligned} \tag{7}$$

The strength of the MGS/ODY orbital perturbations not only depends on the amplitude of the zonal harmonic variations, but also on the orbital characteristics through the semi-major axis a and inclination i (see Eq. (5)). Odd zonal harmonic perturbations are larger for near-polar orbits than for near-equatorial orbits because of the sine of the inclination term in Equation (5). This is opposite for the even zonal harmonics (cosine of the inclination term in Eq. (5)). Because MGS and ODY have near-polar orbits, the odd zonal harmonic variations perturb their motion at a higher level than the even zonal harmonic ones do. That may explain why only the time-variable odd zonal harmonics can be precisely retrieved from the reconstructed orbits of these two spacecraft (Rosenblatt et al. 2010, in preparation). Equation (5) also shows that the odd zonal harmonics perturb ω and e, i.e. perturbations in the orbital plane, while the even harmonics perturb Ω, i.e. out-of-plane perturbations. Because the velocity perturbations of the orbiter are measured through the LOS Doppler shifts, the orientation of the orbital plane with respect to the Earth's line-of-sight plays an important role in the detection of the small perturbations due to the zonal harmonic variations. When the orbital plane is viewed face-on (edge-on) from the Earth, the Doppler data are insensitive to in-plane (out-of-plane) orbital perturbations, and thus to the odd (even) harmonic signals. In addition, Equations (6) and (7) show the lumped combination between the zonal harmonics, indicating that the inclination value governs the lumped coefficient values. Consequently, it is possible to find inclination values, which may help to retrieve the degree-2 and 3 zonal harmonic variations from tracking data of a single orbiter and not the lumped even and odd harmonic variations (Karatekin et al. 2005). For example, for an inclination $i = 49^\circ$ yielding f_4=0, the contribution of the degree-4 zonal harmonics to the ascending node perturbation is removed. In turn, it would allow a better estimation of the δC_{20} from tracking data of a spacecraft with such an orbital inclination (Rosenblatt et al. 2010, in preparation). The expression of orbital perturbations can also be derived for elliptical orbits (such as for the Mars Express, MEX) using Kaula's approach. In that case, the eccentricity entering into the expression of the lumped coefficients in addition to the inclination may help to improve the determination of δC_{20} and δC_{30}, by merging MEX and MGS/ODY tracking data (given that the orbit of the spacecraft can be determined with sufficient accuracy, Rosenblatt et al. 2005). Therefore, merging tracking data from two orbiters with different orbital inclinations and/or eccentricities will definitely help to strengthen the signal of all low-degree zonal harmonic variations, and thus to "*un-lump*" the time-varying gravity harmonic solutions.

In summary, the determination of the time variation of the gravity zonal harmonics is possible and, along with the LOD solutions, some constraints on the global dynamics of the atmosphere may be deduced (see Cazenave & Balmino 1981; Chao & Rubincam 1990; Yoder & Standish 1997; Folkner et al. 1997; Defraigne et al. 2000; Smith et al. 2001; Dehant et al. 2006; Van den Acker et

al. 2002; Sanchez et al. 2004; Karatekin et al. 2005, 2006a,b; Zuber et al. 2007). For example, the wind part and matter part of the contribution to the LOD variations may be separated (the zonal wind contribution is lower than the surface mass distribution, see Sect. 7).

4 TIME VARIATION OF THE GRAVITATIONAL FIELD INDUCED BY THE TIDES

Tides are interesting phenomena as they can be used for the determination of core properties such as the core state and core dimension. The tides indeed depend on the interior structure of Mars, e.g. there are larger tidal displacements for a fluid core. If the tides can be observed, we can determine the contribution from the interior of Mars by knowing the driving force precisely. The tidal force is derived from a tidal potential that is proportional to the mass of the Sun, which is the most important part, and is proportional to the mass of Phobos as well. Representing the distance between Mars and the Sun, d is about 1.5 times the distance between the Earth and the Sun, but Mars' radius r is twice as small as the Earth's radius, so the tidal potential of Mars is about 7% that of the Earth (it is proportional to r^2/d^3). The contribution of Phobos is about one order of magnitude less than the contribution from the Sun, and that of Deimos is about three orders of magnitude less than the contribution from the Sun. As for the Earth, we have diurnal, semidiurnal, and long period tides. All have potential contributions to the orbital changes of a spacecraft orbiting around Mars. However, the geophysical contribution to the tidal changes in the mass repartition is at the limit of the precision that we can get with radioscience at present. The dimension of a liquid core induces changes in the tidal response (the potential field changes due to deformations) of Mars to the gravitational force. The contribution is at a 35% level. Future observations with a better precision and future measurements performed at the surface of Mars with a long-band seismogram will even allow the determination of the tidal deformations of Phobos (see Van Hoolst et al. 2003).

5 MASSES OF PHOBOS AND DEIMOS

The little moons Phobos and Deimos induce effects on the orbit of a spacecraft around Mars. In particular, a small secular drift of the spacecraft orbit is caused by Phobos' mass. Stacking long data-arcs of observations allows the determination of this secular drift and in turn the mass of Phobos (Smith et al. 1995; Rosenblatt et al. 2008a). In addition, if the spacecraft is orbiting in such a way that it passes close to the little moon(s) (a flyby), the acceleration will be high enough to directly see this effect in the Doppler tracking data (see Fig. 8). Such a flyby lasts a few minutes and Doppler tracking data during the typically one hour around closest approach are analyzed to determine the mass. Taking advantage of the higher elliptical Mars Express (MEX) orbit, it is possible to apply both approaches in order to estimate Phobos' GM (see Fig. 9).

Both flyby and secular approaches are needed to fit the spacecraft dynamical model to tracking data (X-band for MEX, S-band for Viking, and C-band for Phobos-2). Together with the volume, the value of the mass of Phobos will allow for deriving the mean density of Phobos, which gives some hints/constraints on its origin. The result indicates macro-porosity (i.e. large spaces of voids) inside Phobos (Rosenblatt et al. 2008b; Andert et al. 2008, 2010).

6 GRAVITY INDUCED BY PARTICULAR TARGETS

A spacecraft orbiting around Mars may pass over a large edifice, such as the volcano Olympus Mons, at the low-altitude pericenter pass of the Mars Express spacecraft. These passes show a large deviation in the trajectory because of the large mass anomalies associated with the edifice (see Fig. 10). Studying this deviation allows the characterization of the region in terms of the degree of compensation of the topography, in terms of the top and/or bottom loading of the underlying lithosphere, and in terms of the density of the topographic load. In particular, the mass of large volcanoes at the surface of Mars induce important gravitational anomalies. From standing on the surface of Mars for

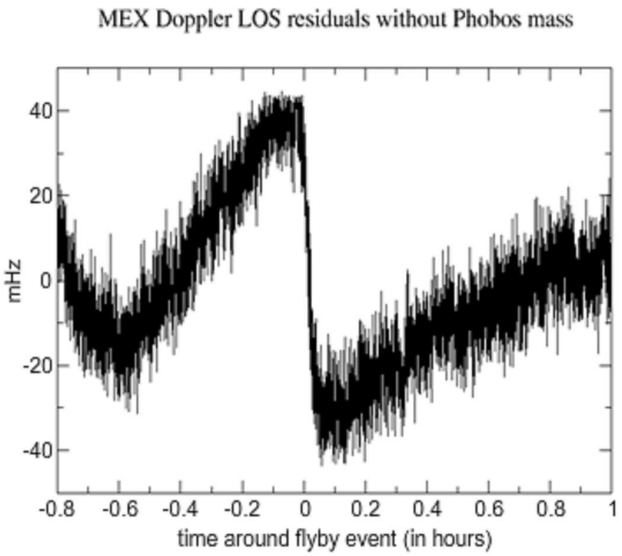

Fig. 8 Phobos mass signal in the MEX Doppler shift measurement expected during a close flyby (closest approach of about 270 km).

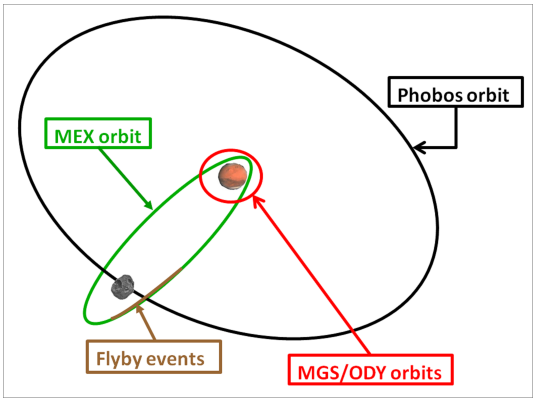

Fig. 9 Schematic representation of the orbits of spacecraft around Mars (in blue-color is represented the time-span used to determine the mass from flyby events).

a very long time, in conjunction with lithospheric properties which allow compensation, the mass of the volcano would be totally compensated by a counterpart root of the edifice (a case of isostatic equilibrium) and almost no gravitational anomaly would be observed above the Martian surface. However in practice, on Mars, the signatures of many topographic features are seen in gravitational effects. The gravitational anomaly of a volcano such as Olympus Mons is indeed only partially compensated by the contributions due to the additional flexure of the lithosphere induced by the volcano (see Fig. 11). The bending of the lithosphere depends on its stiffness, the stress involved, and its material properties. Additional gravitational effects may as well be caused by the presence of a hot spot

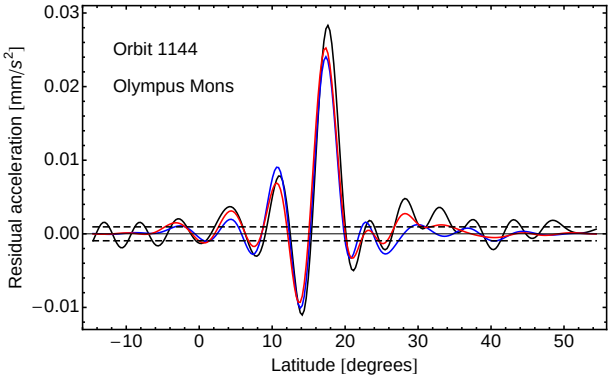

Fig. 10 Acceleration of Mars Express over Olympus Mons derived from one single Doppler tracking pass (*in black*), the same acceleration computed from the gravitational field obtained by the Mars Global Surveyor (MGS) (*in blue*), and the acceleration we would have obtained with a single pass at the altitude of MGS (*in red*). The dotted curve is the noise level in the MEX derived acceleration. Courtesy M. Beuthe.

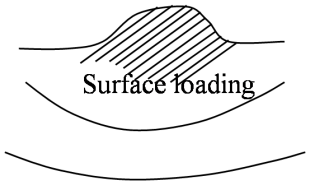

Fig. 11 Flexure of the lithosphere induced by surface loading.

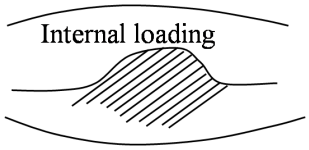

Fig. 12 High gravity induced by internal loading while there is a small topography signal.

or of a large magma chamber beneath the volcano (see Fig. 12). The comparison between gravity and topography thus allows characterizing properties of the crust, the lithosphere and density anomalies below the surface.

A global comparison of topography and gravity maps shows that the Martian topography features, such as the Hellas basin or volcanoes in the Tharsis region are not compensated and may be studied from a relative comparison. These are considered as “targets” to be observed from low pericenter passes of the Mars Express spacecraft. The gravity data on targets are then compared to the computed response of Mars to the loading topography, considering a certain degree of compensation, different crustal densities, and a flexure model for the lithosphere.

The gravity data on targets may be compared as well to the global gravitational field derived from the whole data set by cross-spectral analysis of the line-of-sight accelerations along the orbit. This global gravitational field has been expressed in spherical harmonics up to a certain degree and

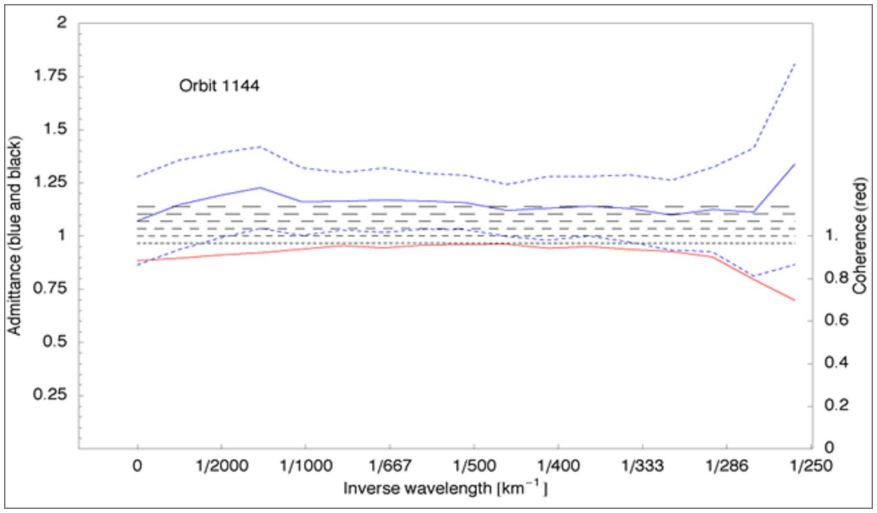

Fig. 13 Admittance (*in blue*) computed for the profile presented in Fig. 10. The blue dashed lines represent the error bars and the horizontal black dashed lines are the admittances expected for different crustal densities with values from 2700 kg m^{-3} to 3200 kg m^{-3}. Courtesy M. Beuthe.

order, which is in agreement with the precision of the available data. Presently, the gravitational field of Mars has been developed up to degree and order 95 (Konopliv et al. 2006; Marty et al. 2009).

The method used to analyze gravity induced by particular targets can be described in three steps. First, using the Doppler shift measurements taken during the pericenter pass, the spacecraft velocity residuals with respect to a determined gravitational field of fixed maximum degree (l_{fixed}), say up to degree and order 50 for instance ($l_{\mathrm{fixed}} = 50$), are filtered with a low-pass filter in order to eliminate some noise and to be able to compute more accurately the acceleration of the spacecraft along the line-of-sight. Second, the acceleration vectors can be predicted from the spherical harmonics of the global field and from the uncompensated topography with a nominal density, at each spacecraft position and projected along the line-of-sight direction. The spherical harmonic coefficients of the topography are computed from the MOLA topographic grid (Smith et al. 2003; Neumann et al. 2004). Third, spectral analyses of the acceleration predicted by the spherical harmonic gravity solution and of the acceleration due to the topography are performed and compared to the acceleration derived from the observed Doppler shifts (see Beuthe et al. 2006). The spectral analysis results are then compared by computing the ratio between the observed acceleration (in the LOS and at the spacecraft altitude) and the same acceleration derived from the topography using a nominal crustal density (2900 kg m^{-3}) in the spectral domain. This ratio is called the gain factor (see Beuthe et al. 2006) and is represented in Figure 13. The observed gain factor spectrum from our target analysis can be compared with the gain factor spectra expected from different local densities (2700 kg m^{-3} to 3200 kg m^{-3}, as represented by the horizontal dashed lines in Fig. 13). More generally, localized admittances between the gravity and the topography can be computed (McGovern et al. 2002). They can be computed as functions of spherical harmonic degree or wavelength and depend on the elastic thickness and on the local density considered in the flexure model. We refer to Wieczorek (2007) for a review of recent results regarding the lithosphere of terrestrial planets. We further mention the recent work of Beuthe (2008) who considered that the elastic thickness of the lithosphere is not homogeneous over the surface of a planet and plays an important role in the flexure mechanism.

Again, as for global gravity, the maximum degree and order $l_{\max}$ of the spherical harmonics is related to the altitude and to the harmonic wavelength through $\lambda_{\min} = 2\pi R/l_{\max}$ (with R being the planetary radius). Note that a spectral analysis of a one-dimensional profile (along the line-of-sight) embedded in a two-dimensional field has the drawback that variations in all directions are projected on the profile, leading to the situation where all possible wavelength contributions are mixed together, including large wavelength contributions that were not expected ($< l_{\text{fixed}}$) (Beuthe et al. 2006).

If gravity and topography are correlated, gravity is considered as being due to loading at the surface and partial compensation involving flexure of the lithosphere as presented in Figure 11.

When the topography is not correlated with gravity, one may consider complete compensation (like the dichotomy of Mars). When the topography-induced acceleration and the gravity are not explained by a flexure model (high gravity signal and small topography signal), internal loading may be present (see Fig. 12).

The admittance for the line-of-sight profile, which is shown in Figure 10, is displayed in Figure 13.

7 MARTIAN EPHEMERIDES

One of the necessary inputs for the computation of precise orbits is the ephemerides of Mars (see Sect. 8). These are of course imperfect and are usually based not only on astrometry but also on the orbiting spacecraft's ranging data. In the Precise Orbit Determination (POD) process, a bias on the ranging measurements is estimated in addition to others parameters. Its estimated value represents the error in the ephemerides (Konopliv et al. 2006; Rosenblatt et al. 2008a). It is near-zero for the period when the spacecraft ranging data had been used for the construction of the ephemerides but it increases for periods when the spacecraft ranging data had not been used. Figure 14 shows the value of this bias with respect to the JPL DE414 ephemerides, estimated using the POD process of different Martian spacecraft.

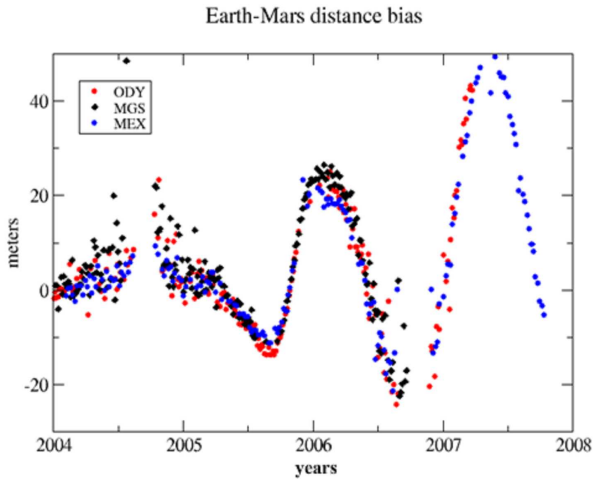

Fig. 14 Error bias with respect to DE414 JPL planetary ephemerides for different recent spacecraft (MEX from Rosenblatt et al. 2008a and MGS/ODY from Marty et al. 2009).

8 MARS ROTATION AND ORIENTATION

The rotation of Mars beneath a spacecraft orbiting around Mars and taking a lander or a rover with it may be seen in the radioscience data. Knowing almost perfectly from Very Long Baseline Interferometry (VLBI) where the Earth is in space, the observation from Earth allows the determination of Mars' rotation and orientation in space. The uniform rotation of the planet must be taken out of the Doppler measurements and the known parts of the orientation of Mars as well. The residuals are then analyzed in terms of the physics of Mars' interior.

8.1 Length-of-day Variations

Mars' rotation around its axis is not uniform due to angular momentum exchange between the solid planet and the atmosphere. There is a variation in the length-of-day which is at the seasonal timescale due to the sublimation and condensation process of CO_2 already mentioned in Section 3. A lander or a rover at the surface of Mars on the equator undergoes huge changes in position of up to 15 m peak to peak over a Martian year (see Fig. 15). This phenomenon can be computed from General Circulation Models (GCM) of the atmosphere. It represents the global seasonal changes in the atmosphere. The angular momentum is transferred to the solid planet by three kinds of coupling mechanisms: (1) the pressure torque related to the atmospheric pressure on the topography, (2) the gravitational torque related to the mass anomalies inside Mars and in the atmosphere, and (3) the friction torque related to the wind friction on the Martian surface (see Karatekin et al. 2010). The angular momentum of the atmosphere consists of two parts: the matter term related to the rigid rotation of the atmosphere with the solid part of Mars which directly involves the surface pressure over all the surface, and the wind term which is related to the relative angular momentum of the atmosphere and directly involves the winds in the atmosphere.

Present day GCMs allow computing the seasonal changes induced in the rotation of Mars as well as in the low-degree gravity coefficients. However, there are still unexplained differences between the computation and the observation. Additionally, the inter-seasonal changes are expected in the time-varying data of the low-degree gravity coefficients due to dust storm contributions, which do not show perfect agreement between observations and the model from GCMs.

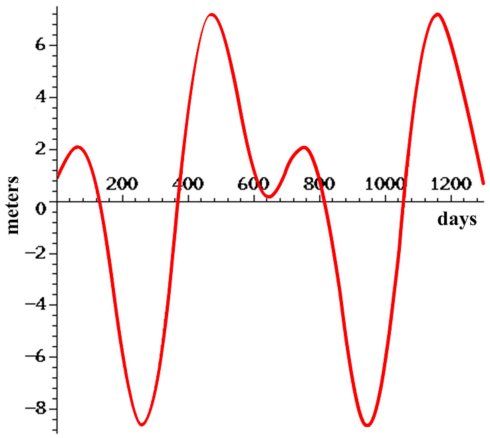

Fig. 15 Length-of-day variations induced by the CO_2 sublimation and condensation process.

8.2 Precession and Nutations

The gravitational attraction of the Sun on the ellipsoidal rotating planet Mars, which is tilted in space with respect to its orbital (≈ ecliptic) plane, induces a torque that tends to rock the equator towards the ecliptic. As Mars rotates, it reacts like a gyroscope and its rotation axis moves with a relatively large amplitude in space around the axis perpendicular to the ecliptic, so it "precesses" in space (see Fig. 16). On this precessional motion is superimposed a series of periodic variations of the orientation of the rotation axis, called nutations. The most important nutation has an amplitude of about 500 milliarcseconds (mas), corresponding to a displacement at the surface of Mars of a few meters (1 mas corresponds to 1.6 cm). The nutational variations in Mars' orientation in space are in two directions: in the direction along the precessional motion and in the direction perpendicular to it, i.e. nutation in longitude $\Delta\psi$ and in obliquity $\Delta\epsilon$, respectively (see Fig. 16). The total displacements at the surface in these two directions are represented in Figure 17. The main nutations have periods of 1 Martian year or are semi-annual or ter-annual or quarter-annual. The nutations are influenced by the interior of the planet. In particular, the presence of an ellipsoidal liquid core induces a resonance in the nutation, called the Free Core Nutation (FCN, see Dehant et al. 2000a,b, 2003; Van Hoolst et al. 2000a,b). This resonance has a period close to the ter-annual nutation for a nominal core (such as 1468 km, the core dimension considered in Sohl & Spohn 1997). The difference between the liquid-core case and the solid core case is shown in Figure 18.

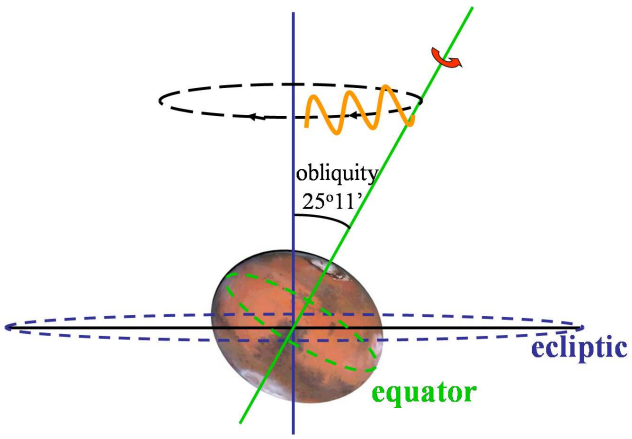

Fig. 16 Representation of the precession (*black*) and nutation (*orange*) motions of the rotation axis of Mars in space.

For a core larger than the nominal case, the FCN period can be very close to the ter-annual nutation, which induces a large amplification in its amplitude. For a smaller core, the FCN period increases, except for the case where an inner core is formed inside the liquid core (which can be the case if the mantle is relatively cold). In that case, the FCN period decreases again when the core size decreases and an FICN (Free Inner Core Nutation) due to the inner core resonance forms. For Mars, nothing is known about the existence of an inner core. There is nevertheless some support for the absence of an inner core from the study of thermal evolution, using knowledge of the remnant magnetic field and the absence of plate tectonics. A large inner core has an effect on the nutations that could be detected using radio observations. Indeed, the amplification of the largest prograde semi-annual nutation due to a liquid core (to the FCN) would be canceled if there were an inner core, but the other nutations amplified by the FCN would almost not change (Van Hoolst et al. 2000a; Dehant et al. 2003; Defraigne et al. 2003). Failure to detect the amplification of the semi-annual

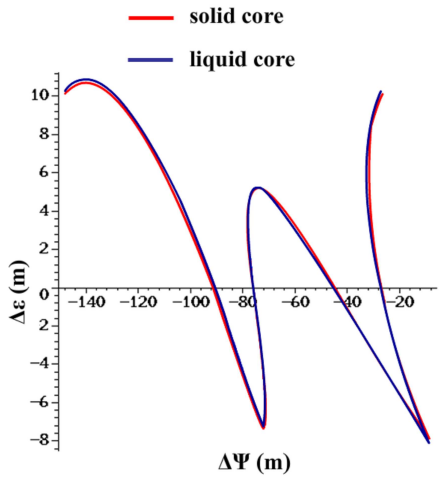

Fig. 17 Amplitude of the nutation represented in a plane perpendicular to the figure axis at the surface of Mars.

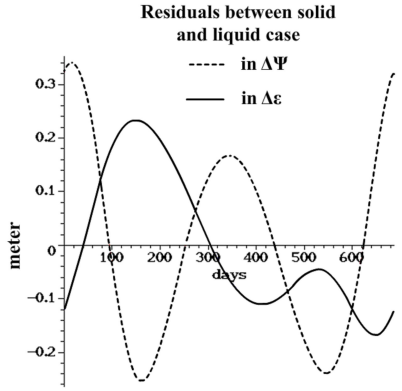

Fig. 18 Amplitude of the nutation represented in a plane perpendicular to the figure axis at the surface of Mars.

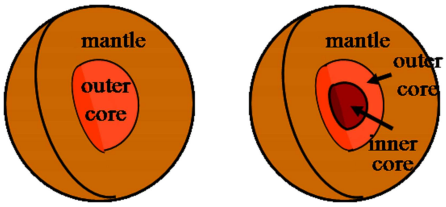

Fig. 19 Sketch showing the interior of Mars with no inner core (*left*) as the nominal case, and with an inner core (*right*).

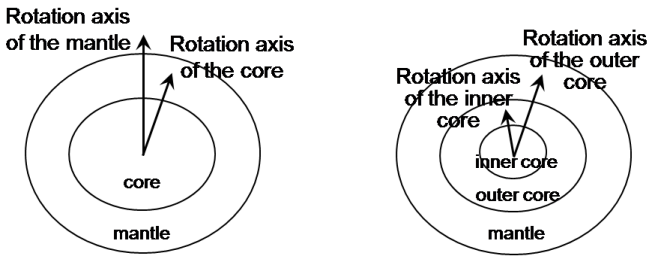

Fig. 20 Sketch representing the FCN (*left*) and the FICN (*right*). For the FCN, one excites a rotation around an axis inside the core, which is not the rotation axis of the mantle; for the FICN, one excites a rotation around an axis inside the liquid core, which is not the rotation axis of the inner core.

nutation with a high precision geodetic experiment (like Lander Radioscience, LaRa, Dehant et al. 2009, 2010; Le Maistre et al. 2010) in its more precise configuration, together with the detection of a liquid core from the retrograde band of the nutations and from the k_2 Love number, could then be interpreted as evidence for a large inner core inside the liquid outer core. The nominal case of a liquid core without an inner core and the case of the existence of a solid inner core are shown in Figure 19. The FCN mode and the FICN mode are represented in Figure 20.

8.3 Polar Motion

Polar motion is the motion of the planet around its rotation axis, or equivalently the motion of the mean rotation axis around the figure axis in a frame tied to Mars. It is induced by the atmosphere and is related to the angular momentum exchange between the atmosphere and the solid planet in terms of the length-of-day variations. One fourth of the atmosphere is participating in the sublimation and condensation phenomenon of the CO_2 in the ice caps. The components of polar motion thus show a seasonal timescale. Additionally, because the rotation axis is not necessarily coincident with the figure axis, there might be a wobble of Mars. This is the so-called Chandler Wobble, which has a period of about 200 d (van Hoolst et al. 2000a,b). Since the atmospheric behavior is not purely harmonic and noise may arise, the Chandler Wobble's contribution to polar motion might be at the level of a couple of meters, depending on the dissipation within the planet (the quality factor of Mars).

The observation of polar motion from radio links between a lander or a rover at the surface of Mars and Earth is only possible for a lander situated at high latitudes; the contributions to the Doppler shift from an equatorial lander are too small to be observable (see Le Maistre et al. 2010).

9 DETERMINATION OF THE PARAMETERS

The observations must be processed with a least squares approach in order to deduce, for example, information about the MOPs or about the orbit of a satellite. A POD procedure using dedicated software is necessary. At the Royal Observatory of Belgium, we use GINS, which stands for Géodésie par Intégration Numérique Simultanée; this software has been developed by the French space agency (CNES) and was further adapted at ROB for planetary geodesy applications.

This software is able to compute a model for all the forces acting on the spacecraft and to numerically integrate its motion. It is also capable of calculating predicted tracking data and performing an iterative least squares process on all sorts of radioscience tracking data in order to adjust parameters related to the data themselves and to the dynamical model of the spacecraft (orbiter or lander) motion. In order to do so, GINS or any other equivalent software uses a series of inputs:

– The tracking data, i.e. Doppler and range tracking data of the spacecraft around planets or on the surface,
– Accelerometer data,
– Ancillary data, i.e. spacecraft attitude, corrections to tracking data (e.g. relativistic and tides effects at tracking stations, ...).

In the case of processing orbiter data, the GINS software performs an iterative least squares fit of a spacecraft's dynamical model on successive data-arcs over one to several-day durations and allows obtaining accurate positioning of the orbiter; it allows obtaining a new orbit (orbiter position and velocity relative to Mars) and post-fit residuals of Doppler and range data. Because it also estimates scale factors for the non-gravitational forces acting on the spacecraft, one can also derive the atmospheric drag and solar pressure effects on the spacecraft. Corrections to the Wheel-off-Loading (WoL) accelerations and estimations of range bias of the Mars-Earth distance are also outputs of the software.

In addition to these outputs, one obtains a normal matrix with information on Martian parameters such as gravitational field coefficients, tides, tidal Love number, rotation parameters of the planet, Martian moon masses, etc., that are estimated.

Table 2 presents a summary of the inputs and outputs of the GINS software for the orbiter case and Table 3 for the lander case. Figure 21 shows the way the Doppler and ranging data are treated.

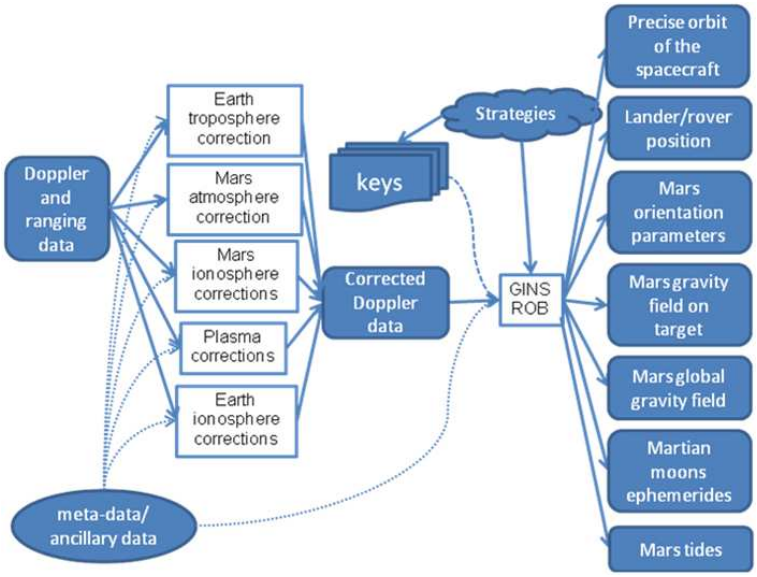

Fig. 21 Schematic use of the Doppler or ranging radioscience data.

From Mars' rotation and orientation parameters or tides or gravitational field, information on the interior of Mars and on the global dynamics of the atmosphere can be found. This approach has already been used by different authors from radio tracking of different orbiting and landed spacecraft (e.g., Smith et al. 1998; Folkner et al. 1997; Konopliv et al. 2006; Rosenblatt et al. 2008a). Recent results from geodesy experiments favor interior models of Mars with a large liquid core and a hot mantle (Yoder et al. 2003; Konopliv et al. 2006) or a smaller liquid core (Balmino et al. 2006; Marty et al. 2009; Rosenblatt et al. 2010, in preparation), depending on the strategy used for processing the data.

Table 2 Inputs and Outputs of the GINS Software for the Orbiter Case

Inputs	GINS	Outputs
Radio data Doppler and range tracking data of spacecraft Accelerometer data Ancillary data - spacecraft attitude (quaternions) - event files (WoL or AMD) - Earth rotation data - Ephemerides of Sun, planets and moons - Position of the center of phase of the antenna - Position of the center of mass of the satellite - WoL amplitudes - Macro model of the spacecraft - Orientation of the solar panels - Albedo of Mars - Atmosphere model of Mars - Position of the Ground stations - Local atmospheric and tidal correction of the Ground stations - ...	Iterative Least Squares fit of a spacecraft dynamical model on successive data-arcs of one to several day duration	- Accurate positioning of orbiter - Normal matrix of the estimated parameters - Post-fit residuals of Doppler and range data - Atmosphere drag scale factor - Radiation pressure scale factor - Range bias on the Mars-Earth distance - Gravitational field coefficients - Time variations of the first low-degree gravity coefficients - Tidal Love number - Rotation parameters of the planet - Martian moon masses - ...

Table 3 Inputs and Outputs of the GINS Software for the Lander or Rover Case

Inputs	GINS	Outputs
Radio data Doppler and range tracking data of spacecraft Accelerometer data Ancillary data - Lander/rover a priori position - Lander/rover tilt - Earth rotation data - Ephemerides of Sun, planets and moons - Position of the center of phase of the antenna - Atmosphere model of Mars - Position of the Ground stations - Local atmospheric and tidal correction of the Ground stations - ...	Iterative Least Squares fit of Mars' rotation and Lander/rover position	- Accurate positioning of lander/rover - Normal matrix of the estimated parameters - Post-fit residuals of Doppler and range data - Rotation parameters of the planet - Tidal Love number - ...

Knowledge of the state of Mars' core and its size is important for understanding the planet's evolution. The evolution of a terrestrial planet and the possibility of dynamo magnetic field generation in its core can be deduced from the physical and thermal states and the dynamics of its mantle and core (see e.g., Longhi et al. 1992; Dehant et al. 2007; Breuer et al. 2007). The state of the core depends on the core temperature, which is related to heat transport in the mantle, as well as on the percentage of light elements in the core (Stevenson 2001; Breuer & Spohn 2003, 2006; Schumacher & Breuer 2006). The present size and state of the core thus have important implications for our understanding of the evolution and present state of Mars (Breuer et al. 1997; Spohn et al. 2001; Stevenson 2001; Van Thienen et al. 2007; Dehant et al. 2007).

Mantle dynamics is also essential in shaping the geology of the surface and in sustaining plate tectonics (Spohn et al. 1998). The radius of the core has implications for possible mantle convection scenarios and, in particular, for the presence of a perovskite phase transition at the bottom of the mantle, which enables global plume-like features to exist and persist over time, i.e., it allows sustained localized upwellings of hot material as might have occurred below Tharsis (Van Thienen et al. 2006). Strong and long-standing mantle plumes arising from the core-mantle boundary may explain the long-term volcanic activity in the Tharsis area. Nevertheless, their existence during the last billion years is uncertain under Martian conditions. Alternatively, Schumacher & Breuer (2006) have proposed that the thermal insulation by locally thickened crust, which has a lower thermal conductivity and is enriched by radioactive heat sources in comparison to the mantle, leads to significant lateral temperature variations in the upper mantle that are sufficient to generate partial melt even in the present Martian mantle. This provides an alternative explanation for Tharsis and its recent volcanism (Neukum et al. 2004).

10 CONCLUSIONS

Radioscience with orbiters around Mars or landers on the surface of Mars allows the acquisition of information on the interior and rotation of the planet. This passes through the knowledge of the precise Doppler and ranging measurements and of precise orbit determination when using spacecraft in orbit. Precise orbit determination demands a lot of efforts as all the gravitational and non-gravitational forces acting on the spacecraft must be considered. Non-gravitational forces such as pressure radiation and atmospheric drag effects on the spacecraft can usually be modeled when ancillary data are provided to the user. Gravitational forces are those which contain the geophysical information that scientists are seeking. In this paper, we have shown that the gravitational forces of the little moon Phobos on the long-term behavior of the orbit of a spacecraft such as Mars Express provide hints on the origin of this little moon. We have also shown that the time variations of the gravitational field provide information on the CO_2 sublimation and condensation process as well as on the tidal deformation of the planet.

The use of landers or rovers will further help to better constrain our knowledge of the interior of the planet and of its global atmosphere as the rotation varies and the orientation changes (the so-called precession and nutation) will be observed using direct radio links from Earth to the surface of Mars. Such experiments are expected in the future.

Acknowledgements This work was financially supported by the Belgian PRODEX program managed by the European Space Agency in collaboration with the Belgian Federal Science Policy Office.

References

Andert, T. P., Pätzold, M., & Häusler, B. 2008, AGU Fall Meeting Abstracts, A1431

Andert, T. P., Rosenblatt P., Pätzold, M., et al. 2010, Geophys. Res. Lett., in press

Balmino, G., Duron, J., Marty, J. C., & Karatekin, Ö. 2006, in Proc. IAG Symposium 2005 on 'Dynamic planet', Cairns, Australia, 125, 895

Beuthe, M., Rosenblatt, P., Dehant, V., et al. 2006, Geophys. Res. Lett., 33, 3203

Beuthe, M. 2008, Geophysical Journal International, 172, 817

Breuer, D., Yuen, D. A., & Spohn, T. 1997, Earth and Planetary Science Letters, 148, 457

Breuer, D., & Spohn, T. 2003, J. Geophys. Res., 108, 5072

Breuer, D., & Spohn, T. 2006, Planet. Space Sci., 54, 153

Breuer, D., Hauck, S. A., Buske, M., Pauer, M., & Spohn, T. 2007, Space Science Reviews, 132, 229

Cazenave, A., & Balmino, G. 1981, Geophys. Res. Lett., 8, 245

Chao, B. F., & Rubincam, D. P. 1990, J. Geophys. Res., 95, 14755

Defraigne, P., de Viron, O., Dehant, V., Van Hoolst, T., & Hourdin, F. 2000, J. Geophys. Res., 105, 24563

Defraigne, P., Rivoldini, A., Van Hoolst, T., et al. 2003, J. Geophys. Res., 108, 5128

Dehant, V., Defraigne, P., & Van Hoolst, T. 2000a, Physics of the Earth and Planetary Interiors, 117, 385

Dehant, V., Van Hoolst, T., & Defraigne, P. 2000b, Surveys in Geophysics, 21, 89

Dehant, V., Van Hoolst, T., de Viron, O., et al. 2003, J. Geophys. Res., 108, 5127

Dehant, V., de Viron, O., Karatekin, Ö., & Van Hoolst, T. 2006, A&A, 446, 345

Dehant, V., Lammer, H., Kulikov, Y., et al. 2007, Space Science Reviews, 129, 279

Dehant, V., Folkner W., Renotte E., et al. 2009, Planet. Space Sci., 57, 1050

Dehant, V., Le Maistre, S., Rivoldini, A., et al. 2010, Planet. Space Sci., accepted

Folkner, W. M., Yoder, C. F., Yuan, D. N., Standish, E. M., & Preston, R. A. 1997, Science, 278, 1749

Karatekin, Ö., Duron, J., Rosenblatt, P., et al. 2005, J. Geophys. Res., 110, 6001

Karatekin, Ö., Dehant, V., & Van Hoolst, T. 2006a, J. Geophys. Res., 111, 6003

Karatekin, Ö., Van Hoolst, T., Tastet, J., de Viron, O., & Dehant, V. 2006b, Advances in Space Research, 38, 739

Karatekin, Ö., de Viron, O., Lambert, S., et al. 2010, Planet. Space Sci., accepted

Kaula, W. M. 1966, Theory of satellite geodesy (London: Blaisdell Pub. Co.), 124

Konopliv, A., Yoder, C., Standish, E. M., Yuan, D.-N., & Sjogren, W. L. 2006, Icarus, 182, 23

Le Maistre, S., Rosenblatt, P., Dehant, V., Marty, J. C., & Rivoldini, A. 2010, submitted to Icarus

Lemoine, F. G., Smith, D. E., Rowlands, D. D., et al. 2001, J. Geophys. Res., 106, 23359

Longhi, J., Knittle, E., Holloway, J. R., & Wänke, H. 1992, in Mars, eds. H. H. Kieffer, B. M. Jakosky, C. W. Snyder, & M. S. Matthewsdel (Tucson: Univ. Arizona Press), 184

Marty, J. C., Duron, J., Balmino, G., et al. 2009, Planet. Space Sci., 57, 350

McGovern, P. J., et al. 2002, J. Geophys. Res., 107, 5136

Moyer, T. D. 2000, Formulation for observed and computed values of Deep Space Network data types for navigation, Monograph 2, Deep Space Communications and Navigation Series

Neukum, G., Jaumann, R., Hoffmann, H., et al. 2004, Nature, 432, 971

Neumann, G. A., Zuber, M. T., Wieczorek, M. A., et al. 2004, J. Geophys. Res., 109, 8002

Rosenblatt, P., Duron, J., Marty, J. C., et al. 2005, AGU Fall Meeting Abstracts, B0149

Rosenblatt, P., lainey, V., Le Maistre, S., et al. 2008a, Planet. Space Sci., 56, 1043

Rosenblatt, P., Le Maistre, S., Marty, J. C., et al. 2008b, AGU Fall Meeting Abstracts, B1377

Rossi, A. P., & van Gasselt, S. 2010, RAA (Research in Astronomy and Astrophysics), 10, 621

Sanchez, B., Haberle, R., & Schaeffer, J. 2004, J. Geophys. Res., 109, 8005

Sanchez, B. V., Rowlands, D. D., & Haberle, R. M. 2006, J. Geophys. Res., 111, 6010

Schumacher, S., & Breuer, D. 2006, J. Geophys. Res., 111, 2006

Smith, D. E., Lemoine, F. G., & Zuber, M. T. 1995, Geophys. Res. Lett., 22, 2171

Smith, D. E., Zuber, M. T., Frey, H. V., et al. 1998, Science, 279, 1686
Smith, D. E., Zuber, M. T., Haberle, R. M., Rowlands, D. D., & Murphy, J. R. 1999, J. Geophys. Res., 104, 1885
Smith, D. E., Zuber, M. T., & Neumann, G. A. 2001, Science, 294, 2141
Smith, D. E., Neumann, G., Arvidson, R. E., Guinness, E. A., & Slavney, S. 2003, Mars Global Surveyor Laser Altimeter Mission Experiment gridded data record, MGS-M-MOLA-5-MEGDR-L3-V1.0, NASA Planet. Data Syst. (Washington D.C.)
Smith, D. E., Zuber, M. T., Torrence, M. H., Dunn, P. J., Neumann, G. A., Lemoine, F. G., & Fricke, S. K. 2009, J. Geophys. Res., 114, 5002
Sohl, F., & Spohn, T. 1997, J. Geophys. Res., 102, 1613
Spohn, T., Acuña, M. H., Breuer, D., et al. 2001, Space Sci. Rev., 96, 231
Spohn, T., Sohl, F., & Breuer, D. 1998, Astron. Astrophys. Rev., 8, 181
Stevenson, D. J. 2001, Nature, 412, 214
Van den Acker, E., Van Hoolst, T., de Viron, O., et al. 2002, J. Geophys. Res., 107, 5055
Van Hoolst, T., Dehant, V., & Defraigne, P. 2000a, Physics of the Earth and Planetary Interiors, 117, 397
Van Hoolst, T., Dehant, V., & Defraigne, P. 2000b, Planet. Space Sci., 48, 1145
Van Hoolst, T., Dehant, V., Roosbeek, F., & Lognonné, P. 2003, Icarus, 161, 281
Van Thienen, P., Rivoldini, A., Van Hoolst, T., & Lognonné, P. 2006, Icarus, 185, 197
Van Thienen, P., Benzerara, K., Breuer, D., et al. 2007, Space Science Reviews, 129, 167
Wieczorek, M. A. 2007, in Treatise on Geophysics, eds. G. Schubert, & T. Spohn (Elsevier), 10, 165
Yoder, C. F., & Standish, E. M. 1997, J. Geophys. Res., 102, 4065
Yoder, C. F., Konopliv, A. S., Yuan, D. N., Standish, E. M., & Folkner, W. M. 2003, Science, 300, 299
Zuber, M., Lemoine, F., Smith, D., Konopliv, A., Smrekar, S., & Asmar, S. 2007, J. Geophys. Res., 112, 5